

ARMY RESEARCH LABORATORY



Processing, Mechanical Properties, and Ballistic Impact Effects of Austempered Ductile Iron

by John F. Chinella, Brian Pothier,
and Martin G. H. Wells

ARL-TR-1741

August 1998

DTIC QUALITY INSPECTED 1

19980911 029

Approved for public release; distribution is unlimited.

The findings in this report are not to be construed as an official Department of the Army position unless so designated by other authorized documents.

Citation of manufacturer's or trade names does not constitute an official endorsement or approval of the use thereof.

Destroy this report when it is no longer needed. Do not return it to the originator.

Army Research Laboratory

Aberdeen Proving Ground, MD 21005-5069

ARL-TR-1741**August 1998**

Processing, Mechanical Properties, and Ballistic Impact Effects of Austempered Ductile Iron

John F. Chinella, Brian Pothier, Martin G. H. Wells
Weapons and Materials Research Directorate, ARL

Abstract

This study describes the resistance to penetration and the damage to austempered ductile iron (ADI) from ballistic impact. The resistance to penetration is determined with an average velocity with a 50% probability for complete penetration, the V-50 ballistic limit. The responses of the ADI material to impact are shown by observations of penetration modes, microstructural changes, and fracture topographies. Mechanical properties and ballistic limits are shown for two variations of the austemper process. ADI targets reveal a capability for multiple impacts without structural failures. Penetration modes include ductile hole growth, radial fracture, petaling, and scabbing. V-50 velocities of ADI with lower values of hardness and strength are equal or greater than the V-50 velocities of ADI with higher values of hardness and strength. Graphite spheroids of this ductile cast iron appear to affect plastic deformation and penetration modes by localizing stresses, microstructural changes, and fracture.

Table of Contents

	<u>Page</u>
List of Figures	v
List of Tables	vii
1. Introduction	1
2. Background	2
2.1 ADI: Processing, Microstructure, and Mechanical Properties	2
2.2 The V-50 Ballistic Test	3
3. Materials and Experimental Details	4
3.1 Processing, Microstructure, and Mechanical Properties	4
3.2 V-50 Test Details	8
4. Experimental Results and Discussion	9
4.1 V-50 Ballistic Limits of APM2 0.30- and 0.50-cal. APM2 Projectiles	9
4.2 Perforation/Failure Modes of Intermediate-Thickness Targets	11
4.3 Experimental Views: ADI Targets and Cross Sections	13
4.4 Microstructural Observations	18
4.4.1 <i>Optical Microscopy: 0.30-cal. APM2 vs. ADI</i>	18
4.4.2 <i>SEM and Optical Microscopy: 0.50-cal. APM2 vs. ADI</i>	22
5. Conclusions	29
6. References	31
Appendix: Supplementary Views of Penetration Mode Fracture Profiles, Topography, and Microstructure Sections	35
Distribution List	43
Report Documentation Page	45

INTENTIONALLY LEFT BLANK.

List of Figures

<u>Figure</u>	<u>Page</u>
1. Protection Criteria for Determination of V-50 Ballistic Limit	1
2. Microstructure of ADI	6
3. Comparison of Experimental ADI Results With MIL-A-12560 RHA Requirements (Protection Criteria)	11
4. Typical Failure (Penetration) Modes of Impacted Plates	12
5. Ballistic-Tested ADI Targets: (a) Target 151; (b) Target 151; (c) Target 189; (d) Target 189; (e) Target 187; and (f) Target 001	14
6. Target Fragments From Penetration Modes of Radial Fracture and Scabbing	17
7. Target and Fragment Cross Sections	18
8. Target and Projectile Core Cross Section	19
9. Microstructural Changes: (a) (1) Shear Band, (2) Wear of Projectile and Target; (3) Along Deformed Nodules (0.30-cal. APM2 Projectile vs. G3 ADI, Target 151 Shot 2, Figure 8); (b) Regions From Figure 9a With Enhanced Levels of Stress ..	21
10a. Fracture Topography: Petal Fragment From Target Back	24
10b. Fracture Topography: Delamination Parallel to Target Surface	24
10c. Fracture Topography: Hinge Region Between Target and Petal Fragment	25
10d. Fracture Topography: Hinge Region Between Target and Petal Fragment	25
11a. Fracture Profile: Back Fragment, Radial Fracture, and Scabbing Shown in Region Near Hinge of Petal Fragment and Target	27
11b. Fracture Profile: Center Fragment, Region Near Hinge of Petal Fragment and Target.	27
11c. Fracture Profile: Center Fragment, Region Nearest Projectile Path	28

<u>Figure</u>	<u>Page</u>
A-1a. Microstructural Changes in Target and Projectile Material During Ductile Hole Growth (See Figure 8)	37
A-1b. Microstructural Changes in Target and Projectile Material During Ductile Hole Growth (See Figure 8)	38
A-2. Fracture Topography of Target Fragment From Radial Fracture and Scabbing ...	39
A-3. Fracture Profile of Target Fragment From Radial Fracture and Scabbing	40
A-4. Fracture Profile of Target Fragment From Ductile Hole Growth and Scabbing ...	41

List of Tables

<u>Table</u>	<u>Page</u>
1. Experimental ADI Process Schedule	5
2. Chemical Analysis (Weight-Percent)	6
3. Tension Test Results at -40° C and 25° C	7
4. Charpy Impact Toughness—V-notched and Unnotched Specimens	8
5. V-50 Results—Protection Limit Criteria	10

INTENTIONALLY LEFT BLANK.

1. Introduction

Austempered ductile irons (ADIs) are an important class of materials with low costs and properties and performance often superior to conventional cast iron or steel materials for applications that require strength, ductility, and wear resistance (Johansson 1977; Shepperdson and Allen 1988; Vaccari 1989).

In comparison to as-cast, normalized, or annealed ductile irons, austempered ductile irons may achieve twice the amount of strength in tension with no loss in ductility or toughness (Gundlach and Janowak 1984; Jenkins and Forrest 1990). In properties of high-cycle fatigue (Johansson 1977; Jenkins and Forrest 1990), ADIs are superior to the ferritic, pearlitic, or martensitic grades of spheroidal cast iron.

Austempered ductile irons have demonstrated reliable service under adverse conditions of shock, impact, and wear. Applications include gears, drive wheels, rollers, slides, and other parts.

ADI has been used for vehicle components in automobiles and military vehicles (Vaccari 1989). New applications of ADI are believed possible where service combines conditions of impact and abrasive or adhesive wear.

Components used for Army applications often include design objectives of ballistic tolerance for prevention of structural failures in service. Mechanical tests cannot replicate conditions of ballistic impact, and mechanical tests cannot reliably predict ballistic performance (Manganello and Abbott 1972). The object of this study is to determine, using the V-50 ballistic-limit test method (U.S. Army Materials Technology Laboratory 1987), the resistance to penetration, and the resultant effects of damage from ballistic impact. Values of V-50 ballistic limits are obtained from tests using plates of ADI matched against armor-piercing (AP) rounds. V-50 values and mechanical properties are shown as the result of two variations of material processing.

2. Background

2.1 ADI: Processing, Microstructure, and Mechanical Properties. The austemper process includes austenitization of cast nodular iron followed by quenching and holding at temperatures in the bainitic range (Kovacs 1991). Austenitization temperatures range between 815° C and 925° C, and austemper temperatures between 230° C and 400° C. To avoid the transformation to pearlite, alloy content must be controlled and section thickness must be limited (Rundman 1991).

The bainitic reaction of ductile cast irons with high-silicon contents differs from that of steels. Carbon rejected by bainitic ferrite during austempering of ADI diffuses within austenite that becomes enriched with carbon. The transformation to stable phases of ferrite and carbide is delayed. This metastable transformation (Porter and Easterling 1984) is called the *stage I* reaction of austempering (Rouns, Rundman, and Moore 1984). After the stage I transformation, the main constituents of the microstructure consists of nodular graphite, and ausferrite, a mixture of acicular bainitic-ferrite and carbon-enriched austenite (Kovacs 1990).

During the bainitic reaction, the austenite absorbs carbon and increases in carbon content, lowering M_s , the temperature of the start of a thermal martensitic transformation. Due to the low M_s , the carbon-enriched austenite that remains is a much more stable and tougher constituent than austenites retained from quenching of steels or irons (Rundman 1991; Shepperdson and Allen 1988).

The completion of the bainitic transformation in high silicon ductile iron occurs with the decomposition of the carbon-enriched austenite into ferrite and carbide. This second stage, *stage II*, occurs at high austemper temperatures or after long periods of time. The second stage of transformation and the resultant microstructure are deleterious to mechanical properties of ductility and toughness.

Austempering at low temperatures yields high-strength material with fine ferrite structures, and a small volume fraction of austenite. As austemper temperatures increase from 230° C to 400° C,

the volume fractions of carbon-enriched austenite obtained increase from about 15% to 50%. The yield and ultimate strengths in tension decrease, and levels of ductility and toughness increase along with higher volume fractions of carbon-enriched austenite. Austempering at the high range of temperatures yields large feathery plates of ferrite (Kovacs 1991).

2.2 The V-50 Ballistic Test. The V-50 ballistic limit (V-50) test method measures the resistance to penetration of armor materials. The V-50 is a statistical velocity, with a 50% probability for complete penetration. The V-50 is obtained from a series of ballistic impacts, at a constant angle of obliquity. The accompanying changes in configuration of the projectile and target are often recorded (U.S. Army Materials Technology Laboratory 1987).

Ballistic impacts during the V-50 test are defined in terms of penetration, the depth or process of travel into the target material (Backman and Goldsmith 1978). Penetration from ballistic impacts is defined as either complete or partial (CP, PP) by criteria of the Army, Navy, and Protection Ballistic Limits (Backman and Goldsmith 1978; Zukas et al. 1982).

The Protection Ballistic Limit (see Figure 1) used in this study is a common method to test armor performance. Under the protection criteria, penetration is defined as complete if after impact the projectile or target fragments have sufficient kinetic energy to penetrate a thin aluminum witness plate placed 6 in behind the target. V-50 ballistic limit test data and military armor specifications are available for many materials under the protection criteria.

A V-50 results from averaging equal numbers of the lowest velocities that result in complete penetrations with the highest velocities that result in partial penetrations. Tests that obtain the V-50 for armor acceptance tests require two, four, or six impacts within a narrow range of test velocities of about 18–30 m/s. The size of the projectile caliber specified for a V-50 test is usually less than or equal to the thickness of the armor.

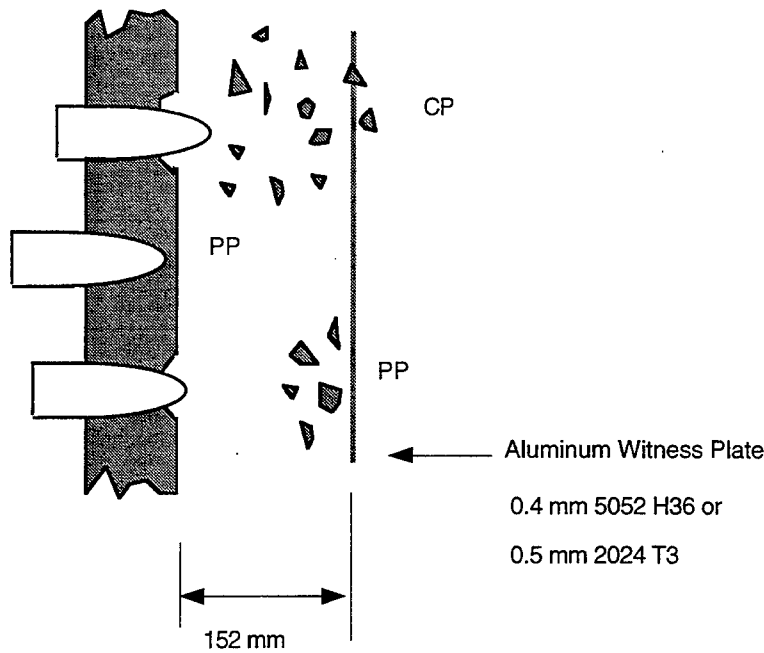


Figure 1. Protection Criteria for Determination of V-50 Ballistic Limit. Complete Penetration (CP), Witness Plate Is Perforated by Either a Fragment of the Plate or the Projectile, Permitting the Passage of Light. Partial Penetration (PP), No Passage of Light Is Visible Through the Witness Plate Whether or Not Perforation of the Target Occurs.

The V-50 test method, or observation of changes in configuration of projectiles and targets, must be used for development and acceptance testing of armor and ballistic-tolerant components. Although tensile strength or target hardness has been found to be consistently indicative of levels of ballistic protection, diverse factors of strain, strain rate, fracture, temperature, and material properties and behavior affect ballistic performance and penetration modes (Crouch 1988). Stress, strain, and fracture are often localized. Predictions of ballistic performance from simple mechanical tests, theories, or analytical methods can be difficult (Manganello and Abbott 1972).

3. Materials and Experimental Details

3.1 Processing, Microstructure, and Mechanical Properties. Two sets of experimental ADI materials obtained from variations of commercial processing by Wagner Castings Company, Decatur, IL, are defined for this study as Grade 1 and Grade 3 (G1, G3). Process schedules are

shown in Table 1. The experimental austemper temperatures were nearly identical, and the resultant microstructures were similar in appearance. A typical ADI microstructure includes spheroidal graphite, acicular ferrite, and austenite (see Figure 2). Analysis of these ADI G1 and G3 materials by Matlock and Krauss (1994) indicate austenite contents of 27 and 19%, respectively.

Table 1. Experimental ADI Process Schedule

Process, Grade 1	
Preheat Stress Relief	593° C, 105 min
Austenitize	891° C, 100 min
Quench and Hold	327° C, molten salt, hold 100 min
Final Hardness	302 Brinell or 32 Rockwell C (HRC)*
Process, Grade 2	
Preheat Stress Relief	593° C, 120 min
Austenitize	885° C, 150 min
Quench and Hold	316° C, molten salt, hold 150 min
Final Hardness	387 Brinell or 42 Rockwell C*

Note: Heat treatments of Grade 1 (G1) and Grade 3 (G3) experimental ADIs with process, times, temperatures, and resultant ADI hardness values.

* HRC values are averages of 82 and 97 data points for Grades 1 and 3, respectively.

Results of chemical analysis are shown in Table 2. Good casting and heat treatment practice, and high-purity materials (Kovacs 1991; Klug, Hintz, and Rundman 1985; Rouns, Rundman, and Moore 1984; Moore, Rouns, and Rundman 1985) are required to produce quality ADIs that meet or exceed the strength and ductility specifications of ASTM A 897, Standard Specification for Austempered Ductile Iron Castings (American Society for Testing and Materials 1993; Jenkins and Forrest 1990). The high purity of these ADIs suggests the possibility for further optimization of strength and ductility by processing and microstructure.

Despite the small differences in the process temperatures and times, there are significant differences of Rockwell C hardness (HRC) values between G1 and G3 specimens (see Table 1).

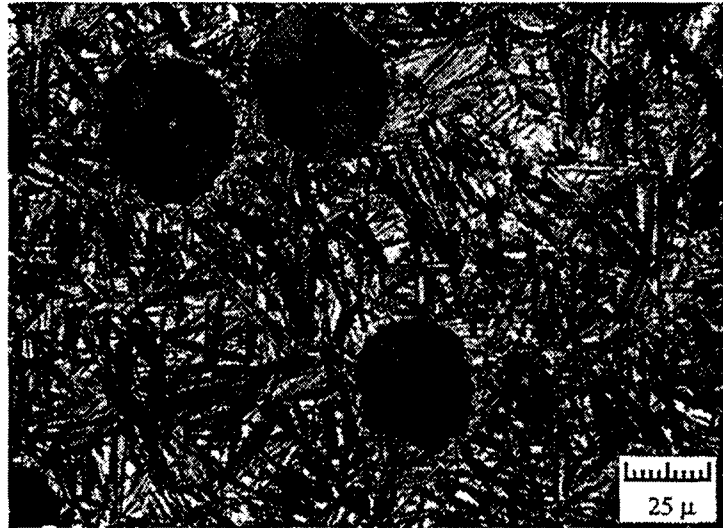


Figure 2. Microstructure of ADI. Structure of G3 ADI Includes Nodular Graphite, Acicular Ferrite, and High-Carbon Austenite. Nital Etch.

Table 2. Chemical Analysis (Weight-Percent)

C	Si	Ni	Cu	Mn	Mg	Cr	Al	S	P	Ti	Mo	Sn	B
3.71	2.72	0.972	0.87	0.27	0.057	0.032	0.015	0.009	0.009	0.005	0.003	0.001	<0.001

Results of tension tests conducted at room temperature and -40°C are shown in Table 3. The results are similar to those obtained for G1 and G3 ADIs by Matlock and Krauss (1994). The ADI of this study has moderate levels of strength and ductility in comparison to all ASTM A 897 strength grades of ADI. The G1 material meets mechanical property requirements of tensile strength, yield strength, and percent elongation, for Grade 150/100/7* of ASTM A 897, except for a deficiency of 5 ksi in tensile strength. Material of G3 meets the mechanical property requirements for Grade 175/125/4* of ASTM A 897, except for small deficiencies in tensile strength (2 ksi) and elongation (0.2%). The average value of elastic moduli at room temperature, 144 GPa, is low in comparison to the elastic modulus of steel (207 GPa). Mechanical property requirements of ASTM A 897 are generally less than ADI strengths and ductilities reported by Gundlach and Janowak (1984).

* Values refer to: tensile strength, minimum (ksi)/yield strength, minimum (ksi)/elongation in 2 in, minimum (%).

Table 3. Tension Test Results at -40° C and 25° C

Test Temperature and Grade	0.2% Y.S. (MPa)	U.T.S. (MPa)	R.A. (%)	El. (%)	E. Mod. (GPa)
G1, -40° C ^a	622	1,079	4.1	6.1	143
G3, -40° C ^b	928	1,284	3.2	5.6	124
G1, 25° C ^b	733	1,003	7.1	9.7	138
G3, 25° C ^b	904	1,190	2.1	3.8	150

^a 0.2% Y.S. averaged from three specimens, all other values averaged from four specimens.

^b Are respective averages of four, five, and six specimens.

Note: Y.S. = Yield Strength, U.T.S. = Ultimate Tensile Strength, R.A. = Reduction of Area, El. = Elongation, E. Mod. = Modulus of Elasticity.

Hardness values are often used to predict tensile strengths of steels. For a steel of 32.2 HRC, the equivalent tensile strength is estimated to be 1,007 MPa, a value achieved by the G1 ADI with an experimental value of 1,003 MPa. For a steel with 41.8 HRC, the equivalent value of tensile strength in tension is estimated to be 1,331 MPa. The divergence of the predicted and experimental values of tensile strengths of G3 material (see Tables 1 and 3) suggests a propensity for fracture during deformation in tension.

At -40° C, G1 specimens have 0.2% yield strength and 0.2% yield strength/elastic modulus (σ_y/E) values less than those at room temperature (see Table 3). The observed reduction of yield strength with decreasing temperature deviates from the flow stress behavior observed in pure body-centered-cubic (BCC) metallic materials (Reed-Hill 1973). A reduction of flow stress at low temperatures is also unusual for BCC or FCC ferrous alloys that contain a large concentration of interstitial elements. With decreasing temperatures, flow stress and yield stress increase in pure BCC materials from a strong dependence on thermally activated components of flow stress.

G3 specimens tested at -40° C have values of 0.2% yield strength that increase above those obtained at room temperature. This increase of flow stress and values of σ_y/E with decreasing temperature is consistent with a FCC or BCC material with a high interstitial content and consistent with materials dominated by thermally activated components of flow stress.

The value of yield stress at -40°C of G1 material is consistent with a controlling mechanism of stress-induced transformation of austenite (Mayr, Vetter, and Walla 1986; Olson 1996) to martensite. At temperatures below M_s^0 , the start-temperature for stress-induced transformation of austenite to martensite, yield stress of metastable austenite decreases in a linear manner and approaches zero at the M_s temperature (Olson and Azrin 1978).

Charpy impact toughness values are shown in Table 4. G1 material has greater impact energy than G3. The impact energy absorbed by unnotched specimens for material of G1 and G3 exceed all ASTM A 897 requirements of impact energy for respective 150/100/7 and 175/125/4 ASTM grades of ADI. In comparison to steels of comparable hardness, all values of V-notch impact energy are low. The low values of V-notch impact energy reveal that ADI material is susceptible to brittle fracture (Reed-Hill 1973).

Table 4. Charpy Impact Toughness—V-notched and Unnotched Specimens

ADI Grade	Impact Energy (Unnotched) (J)	Impact Energy (Notched) (J)
1	122	8.7
3	75	7.0

Note: Values are averaged from 9, 11, 10, and 10 specimens for unnotched and V-notched Grades 1 and 3, respectively.

3.2 V-50 Test Details. Target specimens of G1 and G3 ADIs were impacted at room temperature with APM2 projectiles (AP, hardened steel core). Target plates for the ballistic tests measured $20.32\text{ cm} \times 20.32\text{ cm} \times 1.65\text{--}1.83\text{ cm}$. The target specimens were secured to a target holder with four clamps, each placed at the corners of the target. The resistance to penetration was determined by calculation of a V-50 ballistic limit by the protection criteria (see Figure 1) and MIL-STD-662E (U.S. Army Materials Technology Laboratory 1987). Two target plates (one plate each of G1 and G3) were impacted with 0.30-cal. APM2 projectiles, and five plates (2 of G1 and 3 plates of G3) were impacted with 0.50-cal. APM2 projectiles. Impact velocities were controlled by the weight of propellant loads. Target fragments from impact were collected with the use of Kevlar

cloth draped behind the witness sheet. V-50 values were averaged from velocities of either 2, 4, or 6 fair-impacts. Velocity spreads for calculation of V-50s were held to less than 38 m/s. Penetration mechanisms and damage of the front and back surfaces of each target were recorded by photography. Examination of microstructures and fracture surfaces by optical and scanning electron microscopy (SEM) were made on target sections and fragments of G3 material. The impacted areas examined by optical or SEM were selected upon their included modes of penetration also shown in other impacted areas of the target. Impacted target areas examined were from impacts of 0.30- and 0.50-cal. APM2 projectiles.

4. Experimental Results and Discussion

4.1 V-50 Ballistic Limits of APM2 0.30- and 0.50-cal. APM2 Projectiles. Results of the experimental V-50 ballistic impact tests are shown in Table 5. The targets appear to overmatch the 0.30-cal. APM2 projectile by comparison of V-50 velocities and the maximum muzzle velocity of 841 m/s, which is obtainable with full loads of propellant. The 0.50-cal. APM2 projectile appears to overmatch the ADI targets as shown by comparing experimental V-50s of 459–539 m/s to a full-load muzzle velocity of 896 m/s (U.S. Army Materials Technology Laboratory 1987). G1 and G3 targets, despite the differences in mechanical properties and hardness values, have small differences of V-50 values when matched to a single type of projectile.

When matched against the 0.50-cal. APM2 projectile, G1 ADI with the lower hardness and strengths and the greater ductility and toughness, provided greater V-50 ballistic limits. These results appear different than predicted by a relation of a monotonic increase of ballistic performance with increased hardness (Manganello and Abbott 1972; Crouch 1988). For RHA steel and aluminum armors, the levels of protection often improve with increased levels of hardness (strength), despite an inverse relationship of strength and ductility. Deviations to lower levels of ballistic protection with increased target hardness has been associated with effects from the accompanying changes of material properties and penetration modes (Crouch 1988; Woodward 1988).

Table 5. V-50 Results—Protection Limit Criteria

Test No. and ADI Grade	Projectile APM2 cal. (in)	V-50 (m/s)	HP (m/s)	LC (m/s)	V-50 Spread for No. Shots (m/s, No.)
150, G1	0.30	820	817	817	29 for 6
151, G3	0.30	835	839	831	23 for 6
187, G1	0.50	539	539	540	1 for 2
188, G1	0.50	492	488	491	25 for 4
189, G3	0.50	489	504	475	29 for 2
001, G3	0.50	459	465	451	31 for 4
002, G3	0.50	447	451	429	34 for 4

Note: HP = High Partial, LC = Low Complete.

A primary goal for vehicle and armor design, along with ballistic tolerance, is to obtain the maximum protection per unit weight at minimum cost. Weight efficiency may vary greatly with the mode of penetration, the angle of attack, or the hardness, thickness, and density of the target (Crouch 1988). Ductile irons have densities near 7.11 g/cm^3 (Hughes 1988). A typical density of low-alloy steel used for RHA is 7.83 g/cm^3 . For comparison, experimental V-50 results of ADI and MIL-A 12560 requirements for rolled homogeneous armor (RHA) steel are scaled to areal densities (target thickness \times density) of individual targets (see Figure 3). This comparison indicates that for a unit weight and target area, most steels have greater resistance than the experimental ADI to penetration when matched against the 0.50-cal. APM2 projectile. For target plates of 16.5–17.2 mm in thickness, the ADI appears to provide greater normalized protection against the 0.30-cal. APM2 projectile. Armor of 16.5- to 17.2-mm thickness may defeat 0.30-cal. APM2 projectiles; and MIL-A-12560 V-50 requirements are not specified for target thicknesses greater than 14.4 mm.

Hardness values specified for MIL-A-12560 (U.S. Army Materials and Mechanics Research Center 1984) steel plate with thicknesses of 12.7–19.0 mm are 35.4–40.5 HRC. The hardness values of GI and G3 ADIs (see Table 1) are respectively lower and higher than the hardness range specified for RHA steel.

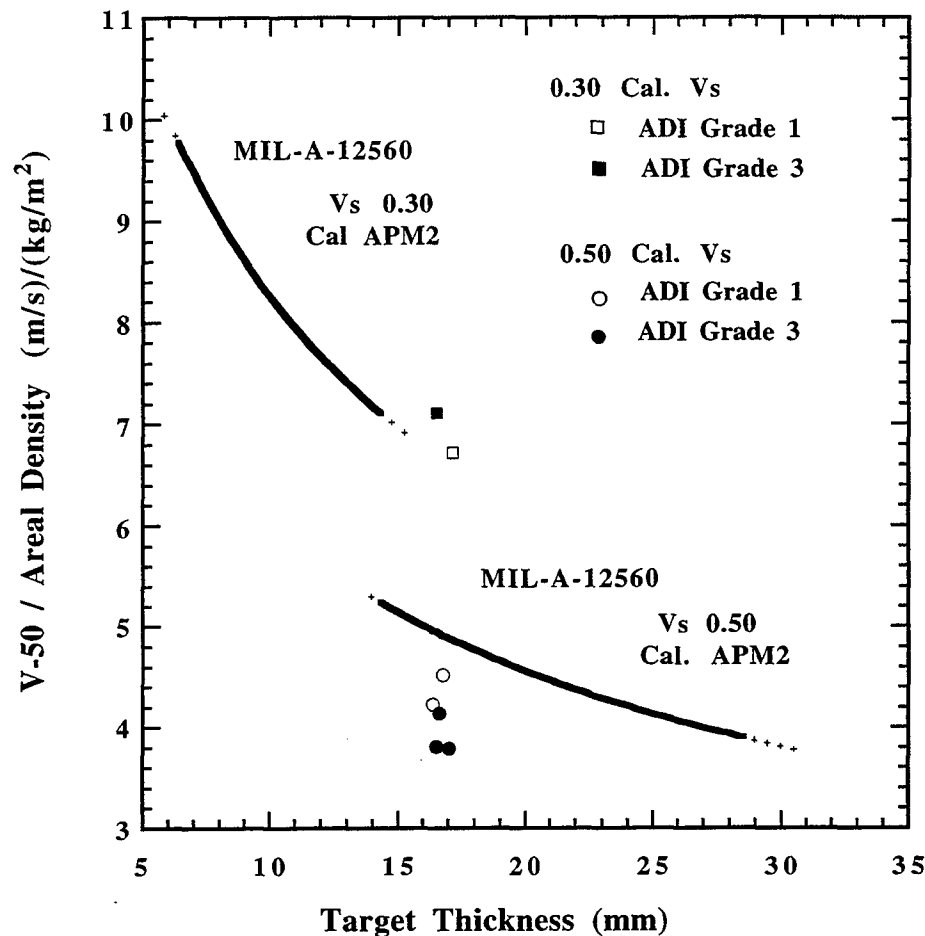


Figure 3. Comparison of Experimental ADI Results With MIL-A-12560 RHA Requirements (Protection Criteria). Scaled to Areal Densities.

4.2 Perforation/Failure Modes of Intermediate-Thickness Targets. Targets fail with penetration (failure) modes that are dependent upon material properties and impact parameters (Backman and Goldsmith 1978; Zukas et al. 1982). The failure modes of impacted plates may include a single dominant mode, or the penetration may be complex, involving several modes. Figure 4 shows penetration modes typical of thin to intermediate thicknesses of targets used in this study. Intermediate thickness targets are defined by the condition that they are affected by stress wave reflections during nearly all events of penetration. The modes are relevant for AP projectiles

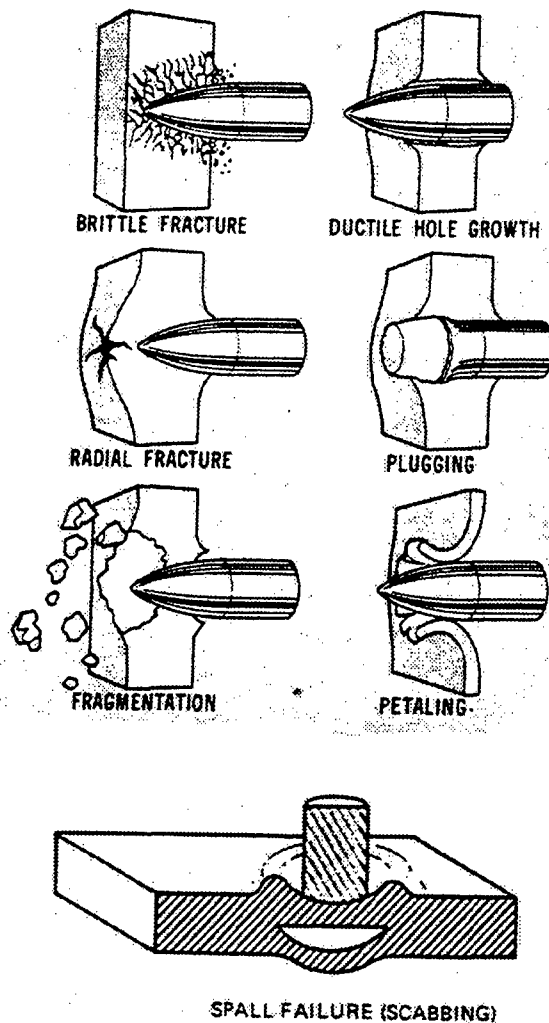


Figure 4. Typical Failure (Penetration) Modes of Impacted Plates (Backman 1976; Backman and Goldsmith 1978).

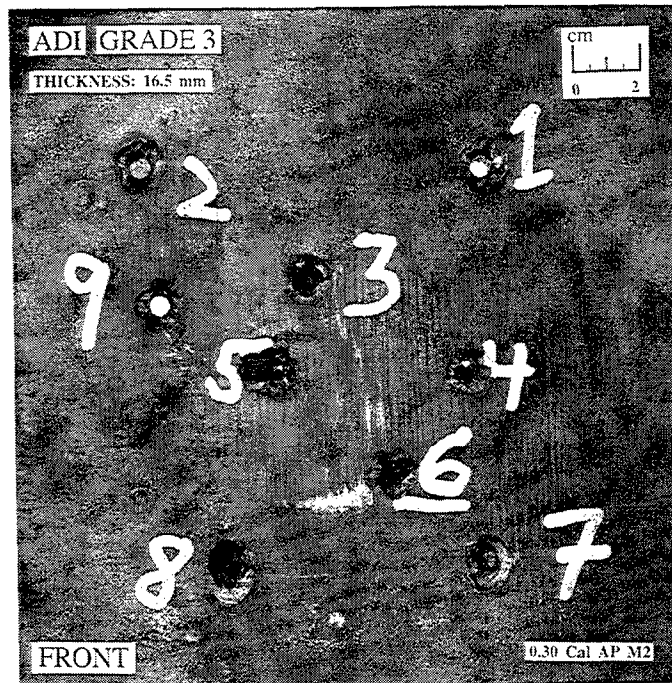
impacting at velocities where material strength, plastic flow, and fracture behavior of the target are important parameters for absorption of kinetic energy.

Spalling occurs as fracture in tension from the reflection of the initial compression wave from the back of the plate or target. It occurs often from intense loads from explosions or impact, particularly in materials stronger or more fracture-resistant in compression than in tension. Fracture by *scabbing*, from delaminating cracks, occurs after passage and reflection of the initial compression wave from the back of the target. Scabbing fractures are accompanied by plastic deformation of

target material and are affected by local material inhomogeneities and anisotropies, such as the roll direction or dendritic structures. Target material may be removed in single or multiple layers. *Petaling* is produced by high radial and circumferential tensile stresses after the initial stress wave. The petal deformation results from bending moments created by bulging through ductile deformation of target material as it is pushed ahead of the projectile. As tensile strength of the target material is exceeded, a star-shaped crack develops around the projectile tip. The sectors formed by petaling may be pushed back if they are not ejected by scabbing.

Ductile hole growth at high levels of hardness is an effective failure mode for energy absorption. Resistance to penetration is greater with higher levels of flow stress. As strength achieved by processing increases, toughness decreases, and at some point failure involves more localized modes of failure that result in lower resistance to ballistic penetration. Localized failure modes include plugging or scabbing of the target and fragmentation of projectiles. Material processed at the highest hardness levels often results in large radial cracks and structural failure of the target (Woodward 1988; Crouch 1988).

4.3 Experimental Views: ADI Targets and Cross Sections. The penetration modes of ADI targets from impact of 0.30- and 0.50-cal. APM2 projectiles (see Figures 5a-f) are complex. Penetration modes include contributions of ductile hole growth, bulging, star-shaped radial fracture, petaling, and scabbing. Star-shaped radial fractures formed on the back of the target after small amounts of bulging. Scabbing formed irregular-shaped craters from the front of the target and removed petal-fragments by crack delaminations of the target. Brittle fracture is defined as the condition of very little plastic deformation of metal during propagation of a crack (Reed-Hill 1973). Although failure modes of radial fracture and scabbing are dependent on crack growth, all target damage remained within three projectile (core) diameters near each impact, and the targets did not undergo structural failure from cracking after eight or nine impacts (see Figures 5a-f). Plugging modes of penetration did not occur with any impact of the target for either projectile.



(a) Target 151.

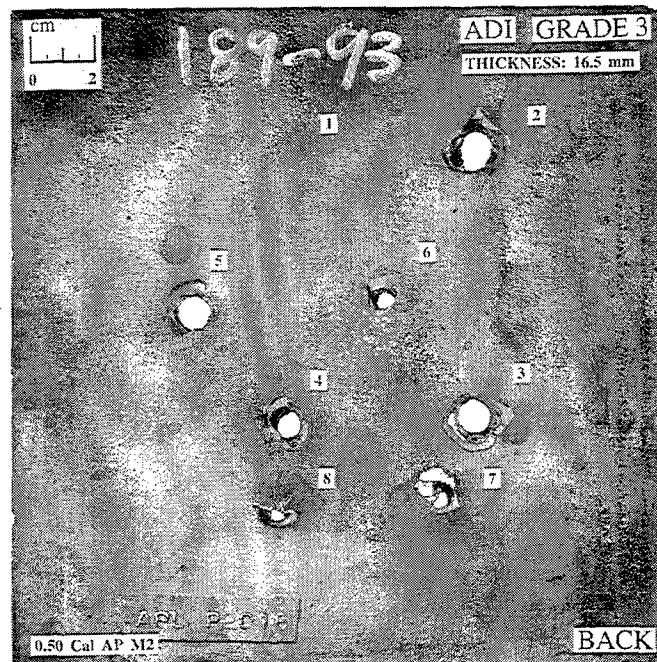


(b) Target 151.

Figure 5. Ballistic-Tested ADI Targets: (a) Target 151; (b) Target 151; (c) Target 189; (d) Target 189; (e) Target 187; and (f) Target 001, Arrows Indicate Casting Defects on Target Surface.



(c) Target 189.

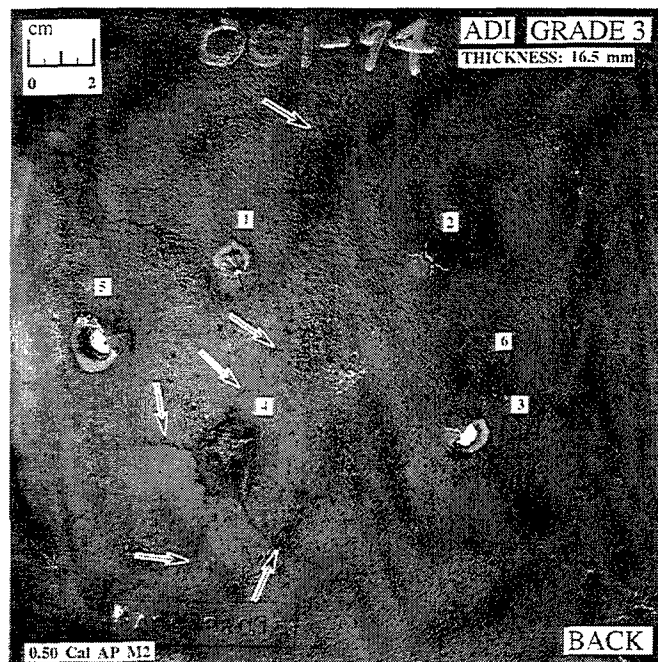


(d) Target 189.

Figure 5. Ballistic-Tested ADI Targets: (a) Target 151; (b) Target 151; (c) Target 189; (d) Target 189; (e) Target 187; and (f) Target 001, Arrows Indicate Casting Defects on Target Surface (continued).



(e) Target 187.



(f) Target 001.

Figure 5. Ballistic-Tested ADI Targets: (a) Target 151; (b) Target 151; (c) Target 189; (d) Target 189; (e) Target 187; and (f) Target 001, Arrows Indicate Casting Defects on Target Surface (continued).

Targets 187 (G1) and 001 (G3) (see Figures 5e-f) have the greatest difference of scaled V-50s. Although the penetration modes of targets 187 and 001 appear similar, target 187 has the greatest V-50 and appears to have a greater amount of plastic deformation about impacted areas. More extensive tests of ADI material with greater ranges of strength and toughness would be required to better correlate mechanical and material properties to penetration mechanisms and ballistic performance.

Target fragments recovered after impact of a 0.50-cal. projectile are shown in Figure 6. The fragments are oriented to match the geometry of damage on the back of the target (see Figure 5d). The two similarly shaped fragments are from outer and interior layers of delaminated target material at one region of the target. The features of star-shaped cracks, radial fracture patterns, and bulging (see Figure 6) are consistent with the penetration modes of radial fracture, petaling, and scabbing. The features shown on the fragments are similar to other impact features shown on the targets (see Figures 5-7).

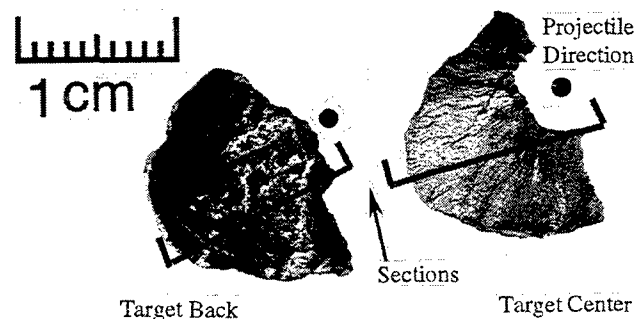


Figure 6. Target Fragments From Penetration Modes of Radial Fracture and Scabbing (0.50-cal. APM2 Projectile vs. G3 ADI, Target 189 Shot 2, Figures 5c-d).

Superposed cross sections of the target, and target fragments shown previously in Figure 6 (see Figure 7), reveal the relative position of the fragments during ballistic penetration. The deformed shape of the fragments is consistent with plastic deformation and bending of target material from penetration and pushing by the projectile. Layers of radial fractures in the target correspond to the initial positions of fragments.

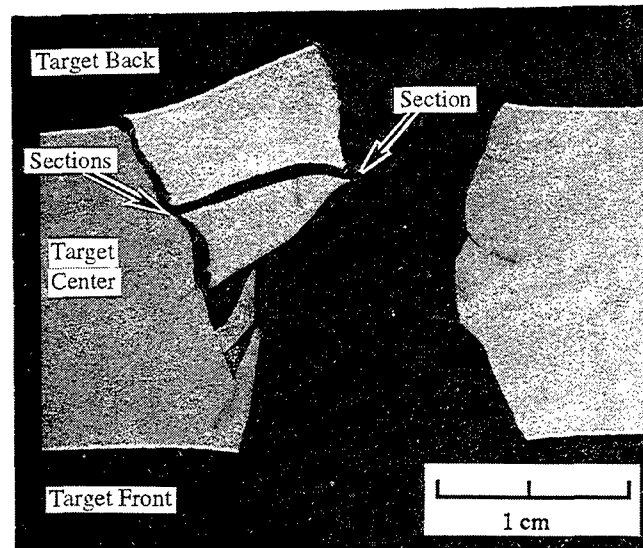


Figure 7. Target and Fragment Cross Sections. Penetration Modes of Ductile Hole Formation, Radial Fracture, and Scabbing (0.50-cal. APM2 Projectile vs. G3 ADI, Target 189 Shot 2, Figure 6). Arrows Refer to Figures 11a–c.

The modes of radial fracture and scabbing (see Figures 5–6) suggest the G3 target material is susceptible to crack dependent modes of failure with brittle fracture, consistent of a material with a greater resistance to fracture under compressive stress rather than stress in tension (Zukas et al. 1982).

A cross section of a 0.30-cal. projectile impact area (see Figure 8) reveals retention of the hardened projectile core in deformed material of the target by a penetration mode of ductile hole formation. Fragments of material from the front and back of the deformed target were removed by scabbing. The penetration of targets with the 0.30-cal. projectile appears to have occurred with a greater contribution of ductile deformation in comparison to penetration of targets by the 0.50-cal. projectile.

4.4 Microstructural Observations.

4.4.1 Optical Microscopy: 0.30-cal. APM2 vs. ADI. Materials deformed at high strain rates, intense loads, and under adiabatic conditions often localize shear in or across narrow bands of

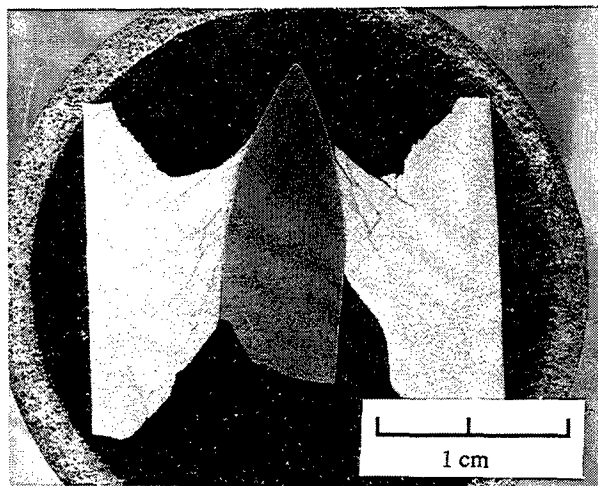


Figure 8. Target and Projectile Core Cross Section. Penetration Mode of Ductile Hole Formation and Scabbing (0.30-cal. APM2 Projectile vs. G3 ADI, Target 151 Shot 2, Figures 5a-b).

material called shear bands. In armors, shear bands are recognized as the result of localized concentrations of stress that propagate across a target faster than the velocity of the penetrator (Zukas et al. 1982; Samuels and Lamborn 1978). Subsequent deformation or fracture occurs along and in the shear bands. The development of shear bands is a significant problem in armor steels that leads to a loss of resistance to penetration (Crouch 1988).

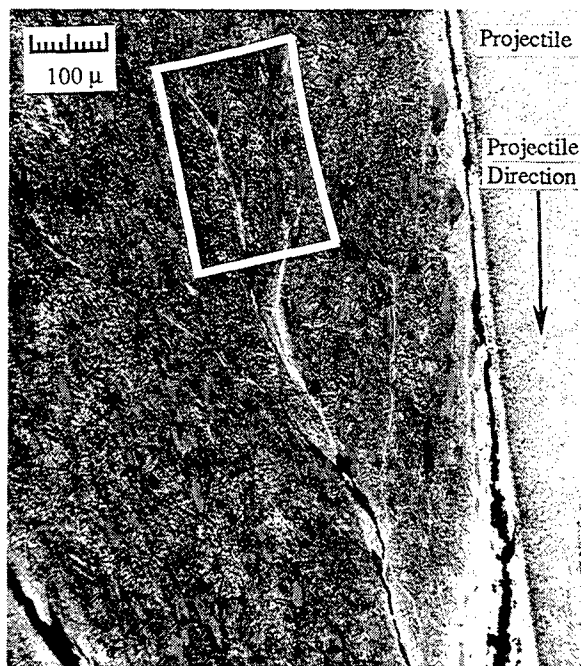
The material changes and etch response of shear bands in steels are dependent on material behavior and the intensity and duration of stress, deformation, and adiabatic heating. Shear bands in steels that etch white are called transformed and are assumed to have undergone austenitization and subsequent martensitic transformation (Samuels and Lamborn 1978). Shear bands that etch are assumed to be deformed. According to Meyers and Wittman (1990), by manipulating the initial microstructure, shear bands in low-carbon steels can be made to produce either deformed or transformed shear bands; and parameters such as thermal diffusivity and critical strains may not truly predict when the deformed-to-transformed shear band event occurs. In comparison to other steel microstructures, Meyers and Whittman (1990) have shown quenched and tempered martensitic steels form the highest densities of shear bands; and quenched and tempered steels most readily form the

transformed, white-etching shear bands. In comparison to a quenched and tempered steel, ausquenched (austempered) steel has been reported to form few shear bands. The penetration resistance provided by bainitic and of martensitic microstructures in low-carbon steel have been reported to be equivalent (Meyers and Wittman 1990).

Studies have shown that the white-etching response results from dissolution of carbides and the inability of etchants to resolve the fine substructures of shear band material (Whittman, Meyers, and Pak 1990). White-etching material of shear bands in quenched and tempered steels has been shown to contain fine-grained martensite (Whittman, Meyers, and Pak 1990). White-etching structures in steels can result from many processes of localized deformation and wear (Whittman, Meyers, and Pak 1990).

Views of the penetration mode of ductile hole formation for the 0.30-cal. projectile (see Figure 8) are shown in Figures 9a–b and A-1 of the Appendix. Large contributions of plastic deformation from ductile hole formation occurred in impacts by the 0.30-cal. APM2 projectile. The shapes of graphite nodules serve as witness markers to the deformation of the target material. Material effects include plastic deformation of the ADI graphite nodules and austenite-ferrite matrix, and localized microstructural changes, or transformation of the microstructure, as suggested by white-etching material. White-etching areas also reveal carbon-enriched austenite of the matrix. Cracks shown in Figure 9a developed from relief of residual stresses during sectioning.

Several forms of microstructural changes resulting in white-etching material appear to have occurred. White-etching regions on and adjacent to the projectile core appear to be effects of high pressures and heating from deformation and wear (see Figures 9a and A-1a). The HRC 60 projectile core is undeformed and shows wear surfaces with white-etching and dark-etching structures. Other, linear-shaped, discontinuous, white-etching regions of microstructural changes suggest the initial development of a shear band. The curvature of the linear shear band reveals that target material has been plastically deformed in the projectile direction.



(a)



(b)

Figure 9. Microstructural Changes: (a) (1) Shear Band; (2) Wear of Projectile and Target; (3) Along Deformed Nodules (0.30-cal. APM2 Projectile vs. G3 ADI, Target 151 Shot 2, Figure 8); (b) Regions From Figure 9a With Enhanced Levels of Stress.

White-etching material in the adiabatically deformed material appears dependent on effects of localized stresses that bridge the close-spaced and elongated graphite nodules. Plastic deformation and microcracking from localized stresses (the bridge effect) occurs during fracture of ductile irons (American Society for Metals 1987). The propagation direction of the white-etching material is opposite the direction of the projectile and of the plastically deformed target material, consistent with a load configuration of shear stress (see Figures 9b and A-1b).

Graphite shape is known to be an important factor in affecting the mechanical properties of cast iron (American Society for Metals 1978). In comparison to other forms of graphite, the nodular shape of graphite in ductile iron provides improvements of strength, toughness, and ductility. Changes in nodule shape during ballistic impact intensify local levels of stress and appear to enhance microstructural changes.

The microstructural effects that propagate from nodule to nodule do not appear to have formed directly by accompanying shear of the adjacent material (see Figures 9b and A-1b). Bainitic ferrite and graphite structures that are separated by the microstructural changes remain continuous and are not sheared. Nodules appear unaffected by nucleation-growth or coalescence of microvoids. The shapes of nodules (indicating the bulk deformation of the ADI) near the leading edge of the microstructural changes do not differ from the nodule shapes farther away. The apparent dependence of the microstructural changes on localized stresses in regions between elongated graphite nodules suggests an effect similar to dynamic recovery (Lee et al. 1993). The absence of shears across the white etching region may be the result of (1) a stress-dependent mechanism that can propagate at much higher velocities than the speed of the projectile and more homogeneous shear of adjacent microstructure; (2) the constraint of adjacent untransformed microstructure; (3) an effect near the end of the period of penetration and deformation. Further investigation by transmission electron microscopy is required to determine the structure and formation mechanisms of white-etching material in ballistically impacted ADI.

4.4.2 SEM and Optical Microscopy: 0.50-cal. APM2 vs. ADI. Scanning electron micrographs (see Figures 10a–d) of a petal fragment shown in Figures 6–7 reveal fracture topographies from

penetration modes of radial fracture and scabbing. A region of the fragment near the back side of the target and the path of the projectile is shown with topography of the penetration mode of star-shaped, radial fracture (see Figure 10a). Fracture features indicate mixed morphologies of ductile and brittle fracture. Features of ductile deformation and fracture are shown by small microvoids and stretching of nodules. Brittle fracture occurred preferentially by localized decohesion and microcracking in weak regions of structure. The fracture morphology that steps among nearest neighbors of graphite nodules is consistent with brittle fracture and localized stress and deformation that bridges graphite nodules (American Society for Metals 1987). Flat, nearly featureless surfaces suggest intergranular brittle fracture along former austenite grain boundaries. The mixed modes of ductile and brittle fracture are consistent with a scabbing mode of failure of armor materials for which fracture stress in tension is less than that of compression.

The fracture topography formed by scabbing (delamination) of the petal fragment from the target (see Figure 10b) reveals small amounts of ductile fracture. Some of the material in this region appears to have been smeared after fracture by wear. There is little evidence of microvoid growth and coalescence on the size scale of the nodules. Microvoid features appear shallow and open on one side. Regions near nodules reveal small amounts of stretching from deformation of the adjacent matrix. The fracture topography appears to follow along a path of stress concentration from nodule to nodule.

The fracture topography of the hinge region of the petal fragment (see Figures 10c and A-2) is located farthest from the projectile's path and approximately 70° from the back surface. The topography includes features of ductile and brittle fracture. Material around nodules is stretched. Brittle fracture appears to have occurred by localized decohesion and cracking of material along close-spaced nodules and prior austenitic boundaries. Fracture features are similar to those shown previously (see Figure 10a) of the radial fracture region nearest the projectile path (see Figures 6-7).

Topography (see Figure 10d) near the back surface of the petal fragment suggests the features were formed by a shear band or void-sheet fracture mechanism (Reed-Hill 1973). Catastrophic crack growth with planar stress states in ductile materials form near-surface features called shear lips.

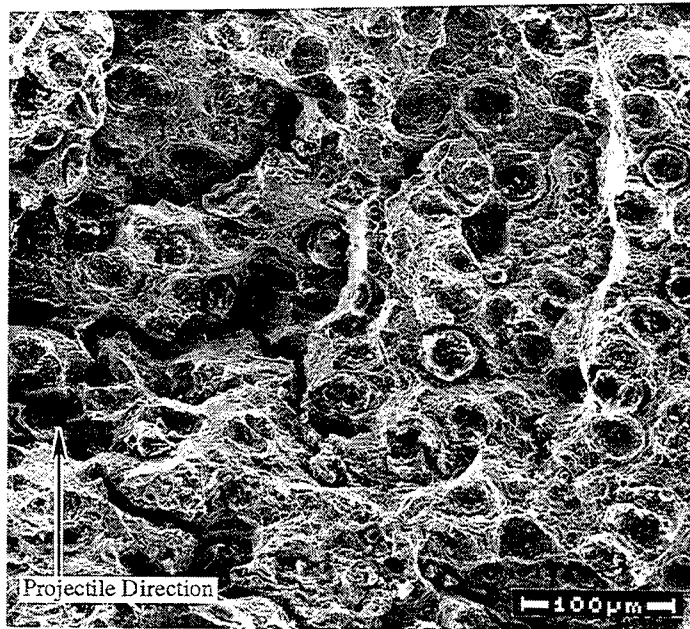


Figure 10a. Fracture Topography: Petal Fragment From Target Back. Near Projectile Path, Star-Shaped, Radial Fracture, Ductile and Brittle Fracture in Tension (0.50-cal. APM2 Projectile vs. G3 ADI, Target 189 Shot, Figures 6–7).

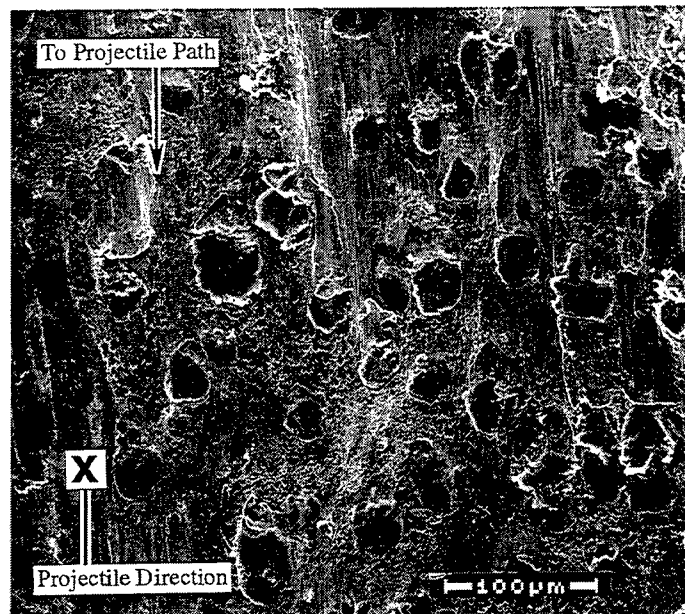


Figure 10b. Fracture Topography: Delamination Parallel to Target Surface. Radial Fracture From Point of Impact. Projectile Direction Into Page (0.50-cal. APM2 Projectile vs. G3 ADI, Target 189 Shot, Figures 6–7).

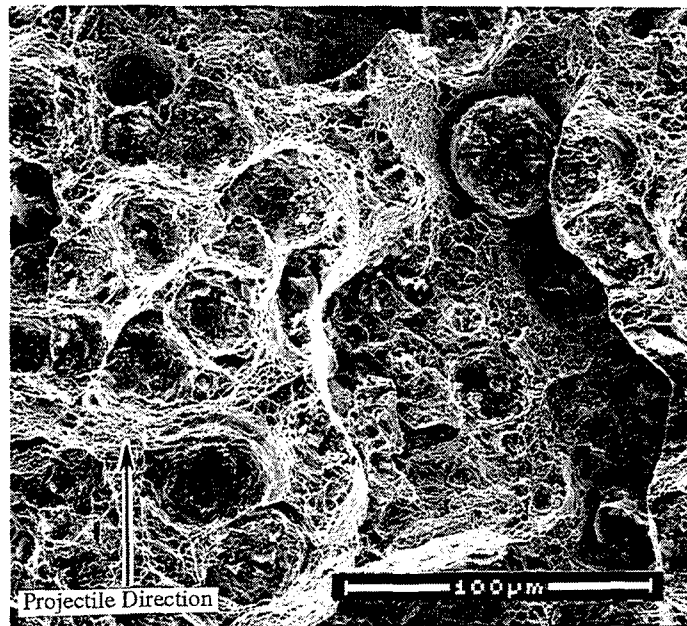


Figure 10c. Fracture Topography: Hinge Region Between Target and Petal Fragment. Ductile and Brittle Fracture in Tension (0.50-cal. APM2 Projectile vs. G3 ADI, Target 189 Shot, Figures 6–7).

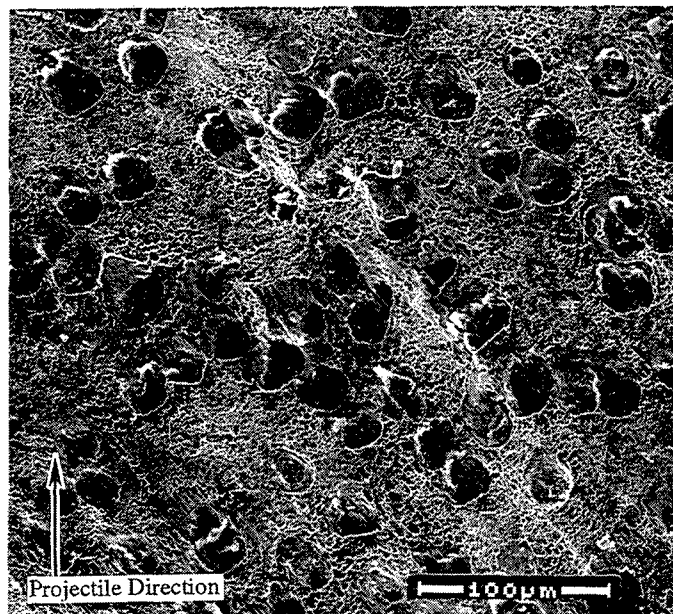


Figure 10d. Fracture Topography: Hinge Region Between Target and Petal Fragment. Ductile Fracture of Shear Lip (0.50-cal. APM2 Projectile vs. G3 ADI, Target 189 Shot, Figures 6–7).

Shear-lip features are not often encountered from fractures formed at quasi-static rates of deformation in cast ductile irons. The shear lip on the fragment appears to be the result of the intense loads and high strain rates from ballistic impact. The topography of the shear-lip region reveals small, shallow, microvoids.

Most of the graphite nodules (see Figure 10d) appear in place, and partially intact, although groups of nodules have been torn away in some regions. The appearance of areas where nodules are relatively intact, and other areas where nodules have been removed, suggests a fracture mechanism that involves localized stresses and crack propagation. Fracture surfaces immediately near clusters of nodules reveal fewer indications of ductile fracture and may correspond to regions subject to enhanced levels of localized stress or microstructural changes.

An order in the distribution of nodules is revealed in three-dimensional SEM views of fracture topography (see Figures 10a–d). The nonrandom distribution is not readily apparent when viewed from ground and polished plane sections. The fracture topographies suggest nodules were formed in dendritic and in flakelike arrangements during eutectic solidification (Jenkins and Forrest 1990). Deformed (see Figure 9b) and flakelike (see Figure 10) arrangements of graphite nodules appear to enhance the localization of stresses, microstructural changes, shear, and fracture during material failure from ballistic impact.

Near-coincident cross sections (see Figures 11a–c and A-3–A-4) of the petal fragments shown previously in Figures 6, 7, and 10 reveal the modes of deformation and fracture among the petal fragments and the target. The regions shown in Figures 11a–b (see Figure 7), farthest from the path of the projectile, intersect between three surfaces of the target and the inner and outer petal fragments. The region shown in Figures 11c and A-4 is the region of the center fragment nearest the path of the projectile (see Figure 7). The shapes of nodules and internal microcracks serve as witness markers that record the loading modes of homogeneous plastic deformation and fracture.

The shapes of deformed nodules between the petal fragments (see Figures 11a–b and A-3) reveal fracture features consistent with Mode II (shear) fracture (Kerlins 1987). The nodule features

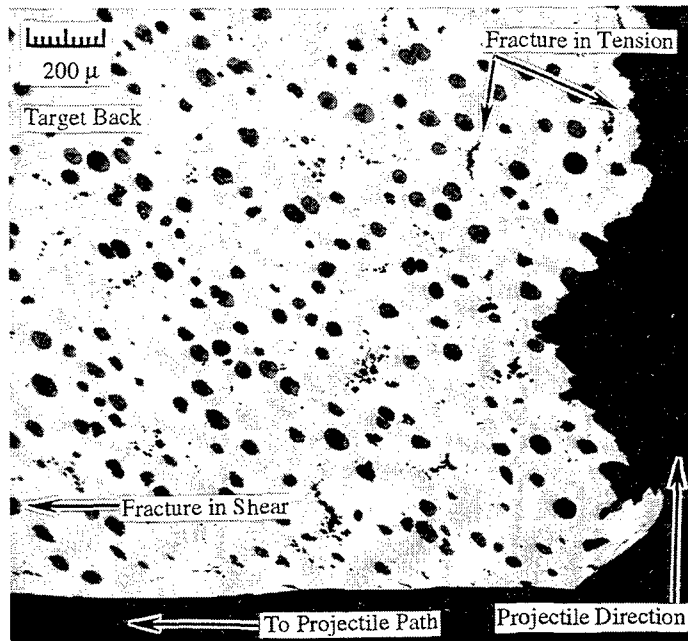


Figure 11a. Fracture Profile: Back Fragment, Radial Fracture, and Scabbling Shown in Region Near Hinge of Petal Fragment and Target. Fractures in Tension and Shear. As Polished.

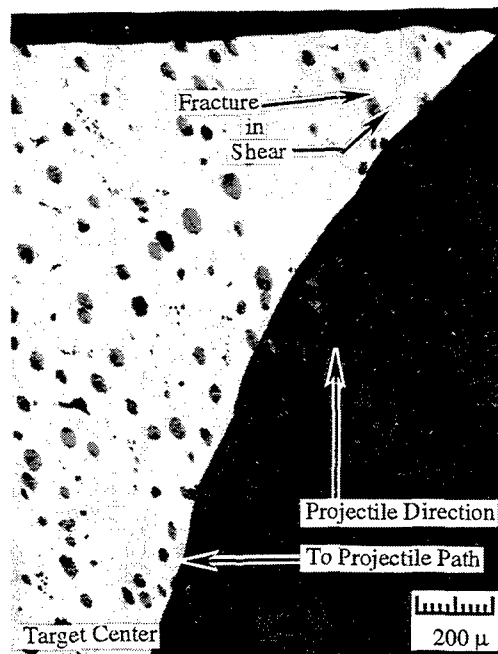


Figure 11b. Fracture Profile: Center Fragment, Region Near Hinge of Petal Fragment and Target. Fractures in Tension and Shear. As Polished.

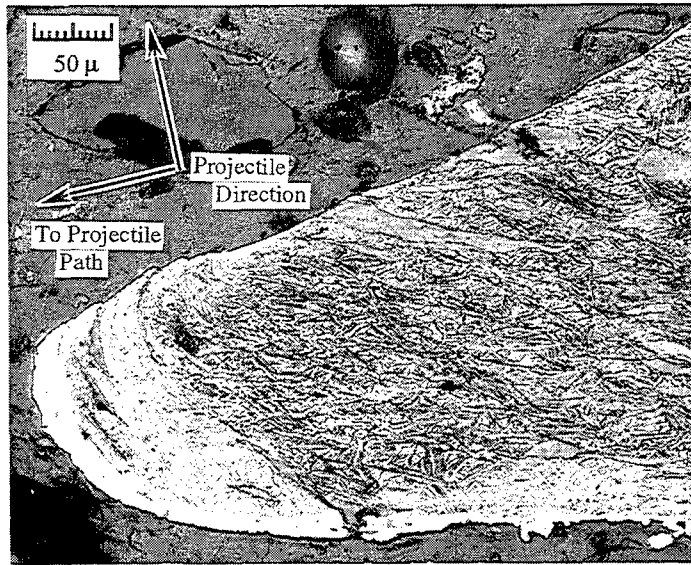


Figure 11c. Fracture Profile: Center Fragment, Region Nearest Projectile Path. Features Suggest Deformation to High Reduction of Area by Shear and Hydrostatic Compression. Nital Etch.

suggest movement of the outermost fragment toward the path of the projectile and movement of the center fragment away from the path of the projectile. A surface on the outer (back) petal fragment farthest from the path of the projectile reveals a mode of fracture in tension (see Figure 11a). This region includes features of ductile and brittle fracture as shown by stretching of nodules and fracture paths that follow close-spaced nodules.

Evidence of brittle fracture is shown in (1) shapes of undeformed nodules along the fracture profile of the outermost fragment; (2) nearly identical shapes of deformed nodules of the interior regions and fractured surfaces of the center fragment.

Features shown in Figures 11c and A-4 include deformed graphite, alignment of acicular ferrite, and microstructural changes. These features and an effective strain equivalent to a high reduction of area appear to have been achieved with shear and extreme pressure in hydrostatic compression.

5. Conclusions

- (1) V-50 velocities obtained with the 0.50-cal. APM2 projectile reveal that ADI targets austempered to lower values of hardness and strength, but greater toughness and ductility, provide greater V-50 velocities than ADI with higher values of hardness and strength.
- (2) In comparisons of V-50s scaled by areal density for the experimental ADI targets (hardnesses of 32 HRC and 42 HRC) and steels of MIL-A-12560 RHA (hardness range of 35.4–40.5 HRC): (a) steels have greater resistance to penetration vs. 0.50-cal. APM2 projectiles; (b) ADI has equal or greater resistance to ballistic penetration vs. 0.30-cal. APM2 projectiles.
- (3) The experimental results suggest ductile irons austempered for further improvements of toughness, ductility, and strain hardening could provide additional improvements of ballistic tolerance and resistance to ballistic penetration. More extensive tests are required to optimize mechanical properties and ballistic performance.
- (4) ADI targets of this study reveal a capability for multiple impacts without structural failures.
- (5) Penetration modes are complex and include contributions of ductile hole growth, radial fracture, petaling, scabbing, and spalling. Material effects from penetration revealed features consistent with ductile and brittle fracture.
- (6) Graphite nodules of this ductile cast iron appear to affect plastic deformation, penetration modes, and fracture features by localizing stresses and microstructural changes. Fracture topographies of impacted targets and target fragments reveal an order in the distributions of nodules consistent with dendritic, or eutectic solidification.
- (7) ADI process methods that achieve more random distributions of graphite nodules during solidification should increase toughness, tensile strength, and resistance to ballistic penetration.

- (8) ADI and projectile material affected by different histories of deformation and stress revealed microstructural changes by etching white. Some microstructural changes of ADI in regions among deformed nodules appeared related to localized stresses and dynamic recovery. The propagation direction of this white-etching material is opposite the direction of the projectile and of the adiabatically deformed target material, consistent with a load configuration of shear stress.

6. References

- American Society for Metals. *Properties and Selection: Irons and Steels*. ASM Metals Handbook, vol. 1, 9th ed., pp. 3-9, 12-71, Metals Park, OH, 1978.
- American Society for Metals. "Ductile Irons, Fractography." ASM Metals Handbook, vol. 12, 9th ed., pp. 228-237, Metals Park, OH, 1987.
- American Society for Testing and Materials. ASTM Subcommittee A04.02 on Malleable and Ductile Iron Castings. "Standard Specification for Austempered Ductile Iron Castings." Designation A 897-90, Ferrous Castings, vol. 1.02, pp. 533, Philadelphia, PA, 1993.
- Backman, M. E. "Terminal Ballistics." NWC TP 5780, Naval Weapons Center, China Lake, CA, 1976.
- Backman, M. E., and W. Goldsmith. "The Mechanics of Penetration of Projectiles Into Targets." *International Journal of Engineering Science*, vol. 16, pp. 1-99, 1978.
- Crouch, I. G. "Metallic Armor-from Cast Aluminum Alloys to High-Strength Steels." *Materials Forum*, vol. 12, pp. 31-37, 1988.
- Gundlach, R. B., and J. F. Janowak. "A Review of Austempered Ductile Iron Metallurgy." *First International Conference on Austempered Ductile Iron: Your Means to Improved Performance, Productivity, and Cost*, pp. 1-12, Metals Park, OH, 1984.
- Hughes, I. C. H. "Ductile Iron." *Casting*, ASM Metals Handbook, vol. 15, 9th ed., pp. 647-666, Metals Park, OH, 1988.
- Jenkins, L. R., and R. D. Forrest. "Ductile Iron." *Properties and Selection: Irons and Steels*, ASM Metals Handbook, vol. 1, 10th ed., pp. 33-55, Metals Park, OH, 1990.
- Johansson, M. "Austenitic-Bainitic Ductile Iron." *American Foundry Society Transactions*, vol. 85, pp. 117-122, 1977.
- Kerlins, V. "Modes of Fracture." *Fractography*, ASM Metals Handbook, vol. 12, 9th ed., pp. 12-33, Metals Park, OH, 1987.
- Klug, R. C., M. B. Hintz, and K. B. Rundman. "Embrittlement of Austempered Nodular Irons: Grain Boundary Phosphorous Enrichment Resulting From Precipitate Decomposition." *Metallurgical Transactions A*, vol. 16A, pp. 797-804, 1985.
- Kovacs, B. "Austempered Ductile Iron: Fact and Fiction." *Modern Casting*, pp. 38-41, March 1990.

- Kovacs, B. "Heat Treating of Austempered Ductile Iron." *American Foundry Society Transactions*, vol. 99, pp. 281–286, 1991.
- Lee, Sunghak, Kyung-Mox Cho, Chang Sun Lee, and Wung Yong Choo. "Microstructural Study of Adiabatic Shear Band Formed by Ballistic Impact in a HY-100 Steel." *Metallurgical Transactions A*, vol. 24A, pp. 2217–2224, 1993.
- Manganello, S. J., and K. H. Abbott. "Metallurgical Factors Affecting the Ballistic Behavior of Steel Targets." *Journal of Materials*, vol. 7, no. 2, pp. 231–239, 1972.
- Matlock, D. K., and G. Krauss. "Mechanical Performance of Austempered Ductile Iron." ARL-CR-117, U.S. Army Research Laboratory, Watertown, MA, April 1994.
- Mayr, P., H. Vethers, and J. Walla. "Investigation of the Stress Induced Martensite Formation in Austempered Ductile Iron." *2nd International Conference, ADI, Your Means to Improved Performance and Cost*, ASME, NY, pp. 171–178, 1986.
- Meyers, M. A., and C. L. Wittman. "Effect of Metallurgical Parameters on Shear Band Formation in Low-Carbon (≈ 0.20 Wt Pct) Steels." *Metallurgical Transactions A*, vol. 21A, pp. 3153–3164, 1990.
- Moore, D. J., T. N. Rouns, and K. B. Rundman. "Structure and Properties of Austempered Ductile Iron." *American Foundry Society Transactions*, vol. 93, pp. 705–718, 1985.
- Olson, G. B., and M. Azrin. "Transformation Behavior of TRIP Steels." *Metallurgical Transactions A*, vol. 9A, pp. 713–721, 1978.
- Olson, G. B. "Hierarchical Adaptive Microstructures: Smart Steels." Final Progress Report 9/1/93-8/29/96, U.S. Army Res. Office Grant DAAH04-93-G-0471, Northwestern University, Chicago, IL, pp. 139–155, 1996.
- Porter, D. A., and K. E. Easterling. *Phase Transformations in Metals and Alloys*. Wokingham, England: Van Nostrand Reinhold (UK), pp. 28–32, 1984.
- Reed-Hill, R. E. *Physical Metallurgy Principles*. Monterey, CA: Brooks/Cole, pp. 786–794, 834–840, 1973.
- Rouns, T. N., K. B. Rundman, and D. M. Moore. "On the Structure and Properties of Austempered Ductile Cast Iron." *American Foundry Society Transactions*, vol. 92, pp. 815–840, 1984.
- Rundman, K. B. "Heat Treating of Ductile Irons." Heat Treating, ASM Handbook, vol. 4, pp. 682–692, Metals Park, OH, 1991.

- Samuels, L. E., and I. R. Lamborn. "Failure Analysis of Armament Hardware." *Metallography in Failure Analysis*, edited by J. L. McCall and P. M. French, New York: Plenum Press, pp. 167-167, 1978.
- Shepperdson, S., and C. Allen. "The Abrasive Wear Behavior of Austempered Spheroidal Cast Irons." *Wear*, vol. 121, pp. 271-287, 1988.
- U.S. Army Materials Technology Laboratory. "Military Standard, V50 Ballistic Test for Armor, MIL-STD-662E." Department of the Navy, Defense Printing Service, Philadelphia, PA, 1987.
- U.S. Army Materials and Mechanics Research Center. "Military Specification MIL-A-12560G, Armor Plate, Steel, Wrought, Homogeneous." Department of the Navy, Defense Printing Service, Philadelphia, PA, 1984.
- Vaccari, J. A. "Why the Interest in ADI Castings." *American Machinist*, pp. 57-60, September 1989.
- Whittman, C., M. A. Meyers, and H. R. Pak. *Metallurgical Transactions A*, vol. 21 A, pp. 707-716, 1990.
- Woodward, R. L. "Materials for Projectile Disruption." *Materials Forum*, vol. 12, pp. 26-30, 1988.
- Zukas, J. A., T. Nicholas, H. F. Swift, L. B. Greszczuk, and D. R. Curran. "Penetration and Perforation of Solids." *Impact Dynamics*, NY: John Wiley and Sons, pp. 155-183, 1982.

INTENTIONALLY LEFT BLANK.

Appendix:

Supplementary Views of Penetration Mode Fracture Profiles, Topography, and Microstructure Sections

INTENTIONALLY LEFT BLANK.



Figure A-1a. Microstructural Changes in Target and Projectile Material During Ductile Hole Growth (See Figure 8). White-Etching Material Appears to Result From: (1) Microstructural Recovery Induced From Stress and Heat Conducted From Wear of Projectile; (2) Wear and Adiabatic Shear; (3) Recovery of Microstructure in Regions of Enhanced Levels of Stress Along Deformed Graphite Nodules. Nital Etch.



Figure A-1b. Microstructural Changes in Target and Projectile Material During Ductile Hole Growth (See Figure 8). White-Etching Material Appears to Result From Recovery of Microstructure in Regions of Enhanced Levels of Stress Along Deformed Graphite Nodules. Nital Etch.

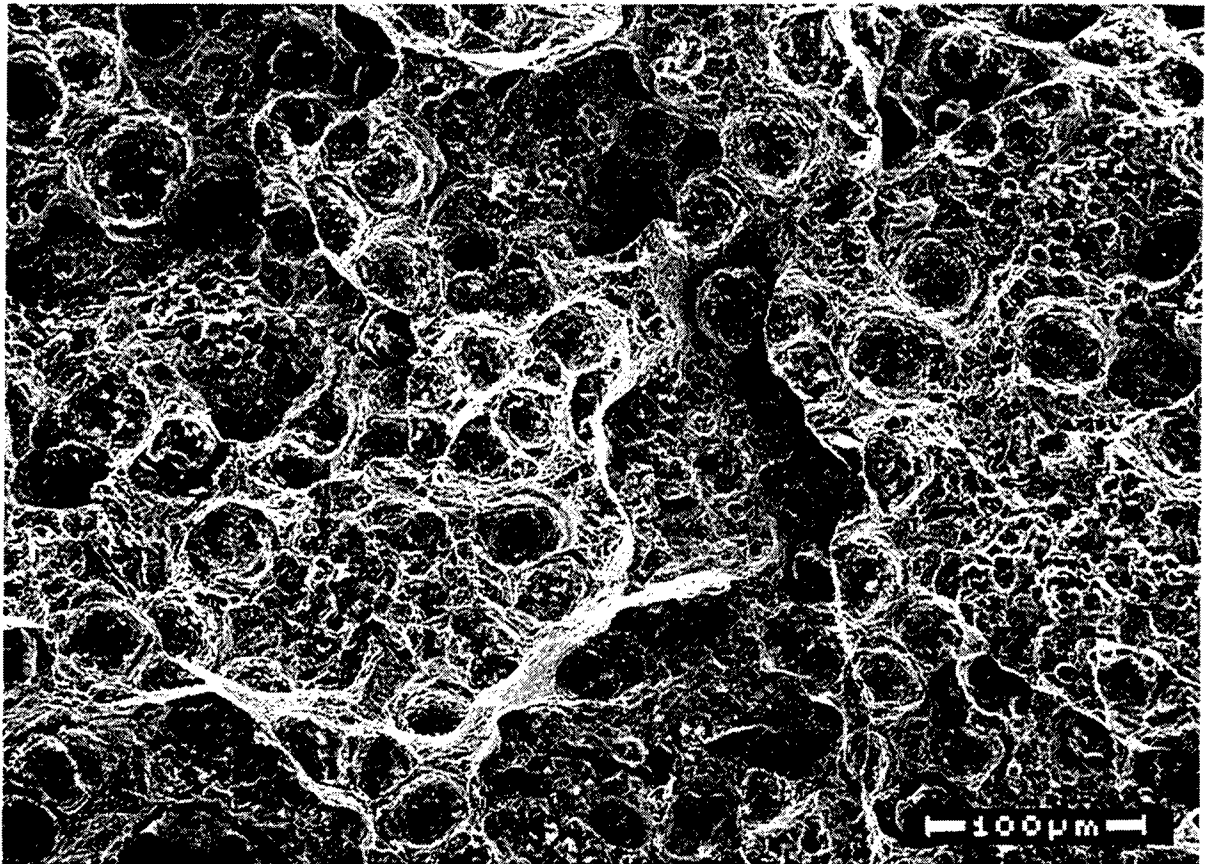


Figure A-2. Fracture Topography of Target Fragment From Radial Fracture and Scabbing. Fracture Morphology Includes Evidence of a Mixed Mode of Ductile and Brittle Fracture in Tension (See Figure 10c). The Stretching of Nodules and Small Dimples Reveal a Ductile Fracture Morphology. The Fracture of Material Through Nodules and Planar Fracture Surfaces Reveal Brittle Fracture. The Fracture Surfaces Appear to Include Dendrite Solidification Structures, and Graphite Nodules Nonrandomly Distributed in Flake-Like Arrangements. The Close-Spaced Nodules Appear to Have Enhanced Fracture From Local Levels of Stress.

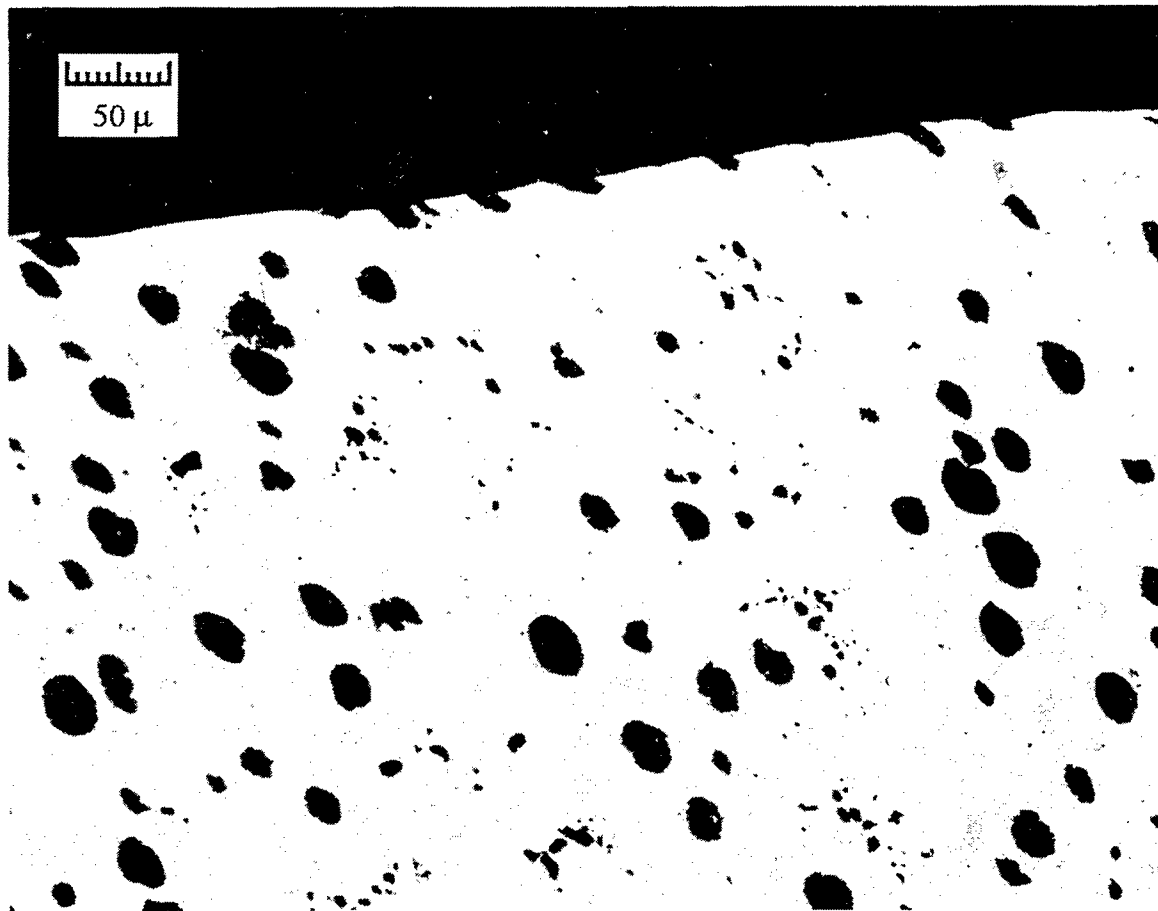


Figure A-3. Fracture Profile of Target Fragment From Radial Fracture and Scabbing. Fracture Path Follows Adjacent Graphite Nodules. Shapes of Nodules Reveal Extent of Deformation and Fracture. View Is Located Midway Between Fragment Hinge and Point of Impact of Center Fragment (See Figure 7). As Polished.

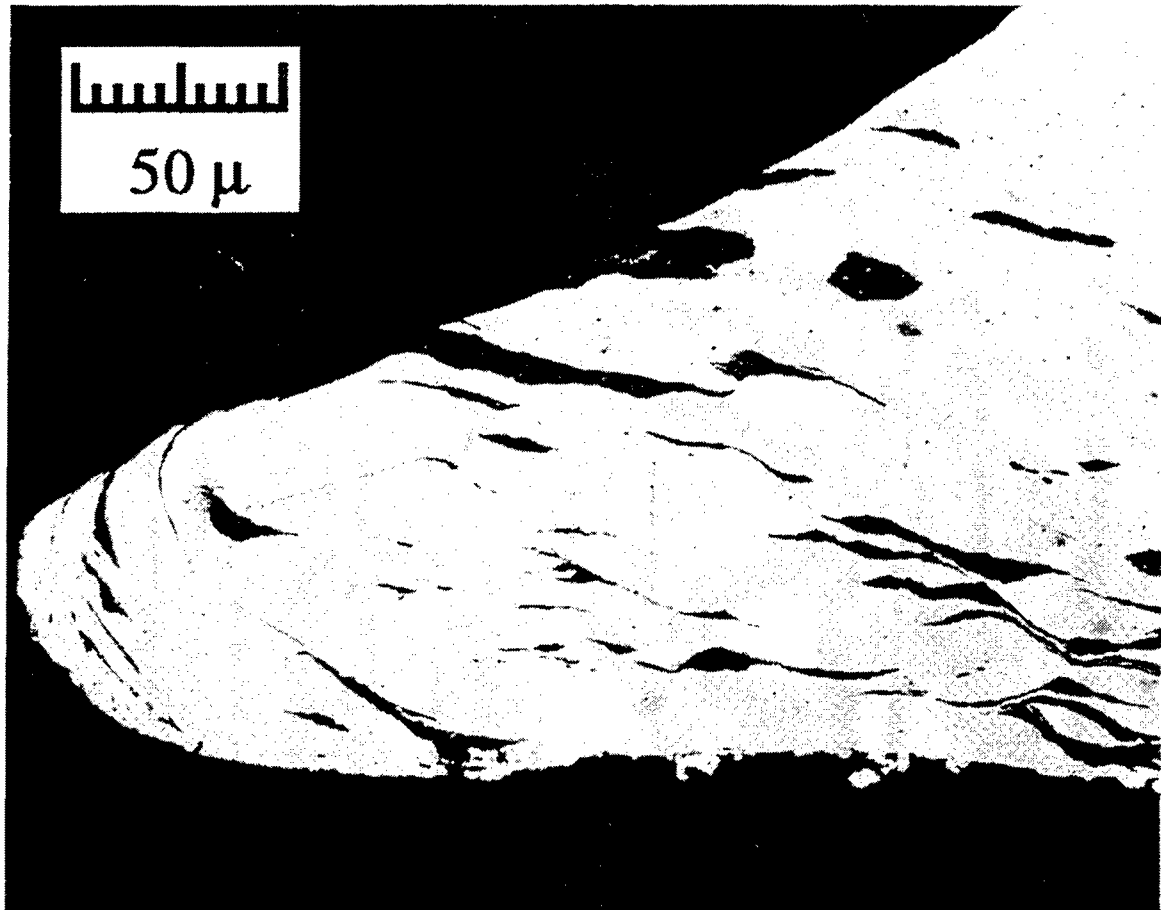


Figure A-4. Fracture Profile of Target Fragment From Ductile Hole Growth and Scabbing. Deformed Graphite Nodules Reveal Evidence of a High Level of Effective Strain Achieved in Shear and Hydrostatic Compression (See Figures 7 and 11c). As Polished.

INTENTIONALLY LEFT BLANK.

NO. OF COPIES	ORGANIZATION
2	DEFENSE TECHNICAL INFORMATION CENTER DTIC DDA 8725 JOHN J KINGMAN RD STE 0944 FT BELVOIR VA 22060-6218
1	HQDA DAMO FDQ DENNIS SCHMIDT 400 ARMY PENTAGON WASHINGTON DC 20310-0460
1	DPTY ASSIST SCY FOR R&T SARD TT F MILTON RM 3EA79 THE PENTAGON WASHINGTON DC 20310-0103
1	OSD OUSD(A&T)/ODDDR&E(R) R J TREW THE PENTAGON WASHINGTON DC 20301-7100
1	CECOM SP & TRRSTRL COMMCTN DIV AMSEL RD ST MC M H SOICHER FT MONMOUTH NJ 07703-5203
1	PRIN DPTY FOR TCHNLGY HQ US ARMY MATCOM AMCDCG T M FIFETTE 5001 EISENHOWER AVE ALEXANDRIA VA 22333-0001
1	DPTY CG FOR RDE HQ US ARMY MATCOM AMCRD BG BEAUCHAMP 5001 EISENHOWER AVE ALEXANDRIA VA 22333-0001
1	INST FOR ADVNCD TCHNLGY THE UNIV OF TEXAS AT AUSTIN PO BOX 202797 AUSTIN TX 78720-2797

NO. OF COPIES	ORGANIZATION
1	GPS JOINT PROG OFC DIR COL J CLAY 2435 VELA WAY STE 1613 LOS ANGELES AFB CA 90245-5500
3	DARPA L STOTTS J PENNELLA B KASPAR 3701 N FAIRFAX DR ARLINGTON VA 22203-1714
1	US MILITARY ACADEMY MATH SCI CTR OF EXCELLENCE DEPT OF MATHEMATICAL SCI MDN A MAJ DON ENGEN THAYER HALL WEST POINT NY 10996-1786
1	DIRECTOR US ARMY RESEARCH LAB AMSRL CS AL TP 2800 POWDER MILL RD ADELPHI MD 20783-1145
1	DIRECTOR US ARMY RESEARCH LAB AMSRL CS AL TA 2800 POWDER MILL RD ADELPHI MD 20783-1145
3	DIRECTOR US ARMY RESEARCH LAB AMSRL CI LL 2800 POWDER MILL RD ADELPHI MD 20783-1145
	<u>ABERDEEN PROVING GROUND</u>
4	DIR USARL AMSRL CI LP (305)

<u>NO. OF COPIES</u>	<u>ORGANIZATION</u>
1	UNITED DEFENSE LP STEEL PRODUCTS DIV VINCENT MATTOX 2101 WEST 10 TH ST ANNISTON AL 36201
1	UNITED DEFENSE LP GROUND SYSTEMS DIV BRIAN H KARIYA 1107 COLEMAN AVE BOX 367 SAN JOSE CA 95103
1	DEPT OF METALLURGICAL & MATERIALS ENGRG MICHIGAN TECH UNIV KARL B RUNDMAN 1400 TOWNSEND DR HOUGHTON MI 49931-1295
1	WAGNER CASTING CO CHARLES CASAD 825 NORTH LOWBER PO BOX 1319 DECATUR IL 62525
1	DEPT OF MATERIALS SCIENCE & ENGRG UNIV OF WISCONSIN-MADISON CARL R LOPER 1509 UNIVERSITY AVE MADISON WI 53706-1596
1	APPLIED PROCESS INC JOHN KEOUGH 12238 NEWBURGH RD LIVONIA MI 48150
1	PRODUCTION BASE MODERNIZATION ACTIVITY FERDINAND DEL CARMEN PICATINNY ARSENAL NJ 07806-5000
1	MICHIGAN TECH UNIV GLENN SIMULA KEEWEENAW RESEARCH CTR HOUGHTON MI 49931

<u>NO. OF COPIES</u>	<u>ORGANIZATION</u>
1	US ARMY TACOM AMSTA TR M MICHAEL BLAIN MAIL STOP 159 BLDG 215 WARREN MI 48397-5000
	<u>ABERDEEN PROVING GROUND</u>
10	DIR, USARL AMSRL-WM-ME, J CHINELLA (6 CP) B POTHIER (2 CP) M. WELLS (2 CP)

REPORT DOCUMENTATION PAGE			Form Approved OMB No. 0704-0188	
Public reporting burden for this collection of information is estimated to average 1 hour per response, including the time for reviewing instructions, searching existing data sources, gathering and maintaining the data needed, and completing and reviewing the collection of information. Send comments regarding this burden estimate or any other aspect of this collection of information, including suggestions for reducing this burden, to Washington Headquarters Services, Directorate for Information Operations and Reports, 1215 Jefferson Davis Highway, Suite 1204, Arlington, VA 22202-4302, and to the Office of Management and Budget, Paperwork Reduction Project(0704-0188), Washington, DC 20503.				
1. AGENCY USE ONLY (Leave blank)		2. REPORT DATE August 1998		3. REPORT TYPE AND DATES COVERED Final, Oct 93 - Sep 94
4. TITLE AND SUBTITLE Processing, Mechanical Properties, and Ballistic Impact Effects of Austempered Ductile Iron			5. FUNDING NUMBERS JONO: 6MPBPR	
6. AUTHOR(S) John F. Chinella, Brian Pothier, and Martin G. H. Wells				
7. PERFORMING ORGANIZATION NAME(S) AND ADDRESS(ES) U.S. Army Research Laboratory ATTN: AMSRL-WM-ME Aberdeen Proving Ground, MD 21005-5069			8. PERFORMING ORGANIZATION REPORT NUMBER ARL-TR-1741	
9. SPONSORING/MONITORING AGENCY NAMES(S) AND ADDRESS(ES)			10. SPONSORING/MONITORING AGENCY REPORT NUMBER	
11. SUPPLEMENTARY NOTES				
12a. DISTRIBUTION/AVAILABILITY STATEMENT Approved for public release; distribution is unlimited.			12b. DISTRIBUTION CODE	
13. ABSTRACT (Maximum 200 words) This study describes the resistance to penetration and the damage to austempered ductile iron (ADI) from ballistic impact. The resistance to penetration is determined with an average velocity with a 50% probability for complete penetration, the V-50 ballistic limit. The responses of the ADI material to impact are shown by observations of penetration modes, microstructural changes, and fracture topographies. Mechanical properties and ballistic limits are shown for two variations of the austemper process. ADI targets reveal a capability for multiple impacts without structural failures. Penetration modes include ductile hole growth, radial fracture, petaling, and scabbing. V-50 velocities of ADI with lower values of hardness and strength are equal or greater than the V-50 velocities of ADI with higher values of hardness and strength. Graphite spheroids of this ductile cast iron appear to affect plastic deformation and penetration modes by localizing stresses, microstructural changes, and fracture.				
14. SUBJECT TERMS ductile iron, austempered ductile iron, mechanical properties, ballistic testing, microstructure			15. NUMBER OF PAGES 48	
			16. PRICE CODE	
17. SECURITY CLASSIFICATION OF REPORT UNCLASSIFIED	18. SECURITY CLASSIFICATION OF THIS PAGE UNCLASSIFIED	19. SECURITY CLASSIFICATION OF ABSTRACT UNCLASSIFIED	20. LIMITATION OF ABSTRACT UL	

INTENTIONALLY LEFT BLANK.

USER EVALUATION SHEET/CHANGE OF ADDRESS

This Laboratory undertakes a continuing effort to improve the quality of the reports it publishes. Your comments/answers to the items/questions below will aid us in our efforts.

1. ARL Report Number/Author ARL-TR-1741 (Chinella) Date of Report August 1998

2. Date Report Received _____

3. Does this report satisfy a need? (Comment on purpose, related project, or other area of interest for which the report will be used.) _____

4. Specifically, how is the report being used? (Information source, design data, procedure, source of ideas, etc.) _____

5. Has the information in this report led to any quantitative savings as far as man-hours or dollars saved, operating costs avoided, or efficiencies achieved, etc? If so, please elaborate. _____

6. General Comments. What do you think should be changed to improve future reports? (Indicate changes to organization, technical content, format, etc.) _____

CURRENT
ADDRESS

Organization

Name

E-mail Name

Street or P.O. Box No.

City, State, Zip Code

7. If indicating a Change of Address or Address Correction, please provide the Current or Correct address above and the Old or Incorrect address below.

OLD
ADDRESS

Organization

Name

Street or P.O. Box No.

City, State, Zip Code

(Remove this sheet, fold as indicated, tape closed, and mail.)
(DO NOT STAPLE)

DEPARTMENT OF THE ARMY

OFFICIAL BUSINESS

BUSINESS REPLY MAIL

FIRST CLASS PERMIT NO 0001,APG,MD

POSTAGE WILL BE PAID BY ADDRESSEE

DIRECTOR
US ARMY RESEARCH LABORATORY
ATTN AMSRL WM ME
ABERDEEN PROVING GROUND MD 21005-5069

NO POSTAGE
NECESSARY
IF MAILED
IN THE
UNITED STATES

